Numerical Methods in Civil Engineering

Thermo-mechanical behavior of shape memory alloy made stent- graft by multi-plane model

S.A. Sadrnejad *

ARTICLE INFO

Article history:
Received:
September 2013.
Revised:
December 2013.
Accepted:
January 2014.

Keywords:
Aneurysm; stent-graft; materials; constitutive model; multi-plane; thermo-mechanical properties.

Abstract:

Constitutive law for shape-memory alloys subjected to multi-axial loading, which is based on a semi-micromechanical integrated multi-plane model capable of internal mechanism observations, is generally not available in the literature. The presented numerical results show significant variations in the mechanical response along the multi loading axes. These are attributed to changes in the martensitic variants nucleated in response to the directionality of the applied loading, as well as to micro-structural texture/fabric present in the multi-planes showing different orientations at any single point through the material. Numerical simulations suggest that the characterization and modeling of the microstructure is of paramount importance in understanding the phenomenology of the thermo-mechanical behavior of shape-memory alloys that are used in manufacturing of stents.

The Niti-S Biliary Stent is a self-expanding uncoated tubular prosthesis designed to maintain patency of bile duct strictures caused by malignant tumors. It consists of a self-expanding thermo-mechanical metal stent. The biliary stent is made of Nickel Titanium alloy (Nitinol) wire, which expands at body temperature. The stent is deployed with supplied introducers for percutaneous and endoscopic use. The existing endoprostheses differ in several aspects, such as shape design and materials. The Niti-S Biliary Stent (NNN) is only indicated for the palliation of malignant structures in the biliary.

This paper aims to propose a capable multi-plane thermo-mechanical model predicting relevant information to understand the principles of stent-grafts behavior and even to develop new method for the correct use of this device. Hence, the use of a stent-graft is based on different characteristics are predicted, and the significant features of an ideal device can be pointed out. Additionally, the materials currently in use to fabricate this type of prosthesis controlled and checked and consequently new materials may be suggested.

1.Introduction

Modeling the three dimensional thermo-mechanical behavior of shape memory alloys and analyzing these special materials and making a possibility of visualizing internal deforming mechanism, a simple constitutive integrated model, named multi-plane, is proposed. The model deals with just shear on plane component and also it's orientation in several planes as well. In the case of static constraint, the shear on plane stress components and corresponding orientations could be obtained by transferring the stress tensor. Then to calculate the on plane deformations, a plane constitutive law is needed to obtain on plane strains. Finally the strain tensor could be obtained by superposing of on plane elastic and inelastic deformations.

Shape memory alloys are widely used for many variety applications such as medical devices and energy absorption and aero space industries and even recently structural engineering. These materials exhibit a strongly nonlinear thermo-mechanic behavior due to abrupt changes in their lattice structure called martensite phase transformation.

The lattice structural phases in high and low temperatures in these materials are respectively called

**Corresponding Author: Professor, Civil Engineering Department ,K.N. Toosi University of Technology, Tehran Iran. Email: sadrnejad@kntu.ac.ir*

austenite and martensite. The ability to transform into each other in different stresses and temperatures and consequently change of mechanical and electrical properties of these materials has encouraged researchers to use these alloys in smart structures.

The ability of returning into the initial shape through increasing the temperature after pseudo plasticity deformations in some temperatures below critical temperature, called *shape memory effect*, is one of the most distinctive features of these alloys. To this reason, these alloys are called shape memory alloys.

Another notable phenomenon is super elasticity in which Increase of the stress imposed on material in high temperature will turn the austenite phase into martensite phase and causes pseudo plasticity deformations. In this case after unloading, the martensite phase will be returned into austenite phase.

For analyzing the structures made by these materials, a simple suitable 3D model is required so that it should be able to predict complicated behavior of one point of these materials under multi axial loading conditions.

An aneurysm, also known as aneurism, is a bulge in a weakened portion of a blood vessel wall much like the bulge that results from over-inflating a tube. Generally, an aneurysm can be defined as a permanent and irreversible localized dilatation of an artery, having at least a 50% increase in diameter compared with the normal one [1].
Aneurysms occur most commonly in the aorta, as well as in arteries located at the base of the brain and in the legs. If left untreated, they may burst or rupture causing a hemorrhagic stroke – in the case of brain aneurysms – or, when located in the aorta or other abdominal vessels, hipovolemic shock, and even death, due to massive blood loss.

Endovascular aneurysm repair, or EVAR, is a percutaneous minimally invasive procedure in which an endoprosthesis, i.e., a stent-graft, is guided from the femoral artery to the affected artery segment. The objective of this procedure is to shield the aneurysm sac from the blood pressure and, thus, prevent the excessive deformation that leads to rupture of the artery wall.

Pre-evaluation of stent-graft deformation limits is one of the key elements in the EVAR's success. In the first applications, the devices were designed individually for the patient but, presently, several different devices, which have different sizes, can be designed and are made of distinct materials, are available. The introduction of such devices increased the availability of EVAR, allowing the selection of the appropriate device for each patient and/or pathology [2]. Although there are several publications describing the devices currently available in the market and the features that stent-grafts should include, there is no document that approaches the properties of the materials used. Thus, this papers intents to fill this gap. The information gathered here allows an enhanced comprehension of stent grafts as well as establish guidelines for improving them.

The proposed simple model is capable of predicting the value and direction of strain tensor for one point of these materials under every 3D proportional and nonproportional loading.

To represent the capability of this model, the predicted different test data in biaxial loading path are compared qualitatively with the experimental results. In these test results the shape memory alloys behaviors such as: super elasticity, asymmetry in tension and pressure, different proportional tension-shear and tension-compression biaxial loading and unloading, and also deviation from normality due to non-proportional tension-shear biaxial loading and unloading, are investigated and presented. The interesting well accuracy of results proves the strength and capability of the proposed model.

2. Stent- Grafts

A stent-graft is an endoprosthesis classified as a class III medical device both in Europe and in the USA. It can be defined as a tubular device composed of a flexible membrane, i.e., a graft, supported by a rigid structure. The skeleton, called the stent, acts as an arterial attachment mechanism and provides structural support to both the graft and the treated vascular segment. The graft forms a new conduit that protects the diseased artery from the pulsatile blood pressure.

These medical devices have been used in the treatment of aneurysms, aortic dissection, trauma and occlusive pathologies. According to the illness and the deployment site in which they are applied, their requirements as well as their design differ. Table 1 presents a classification based on different characteristics such as shape, deployment technique, and fixation method.

Regardless of the shape, stent-grafts present distinct combinations of proximal and distal ends as Fig. 2 illustrates. However, the design of the stent-graft has implications for the deployment site and influences the sealing performance and the migration resistance. For example, when selecting a stent-graft for an aneurysm with a short neck or a tortuous anatomy, the selected device should have a small first covered spring because such a design does not compromise the sealing and assures full apposition of the device. If the device is to be deployed near a peripheral artery, a device whose termination does not interrupt the blood flow, e.g., scalloped flares (Fig. 2a) or bare stent (Fig. 2f), is preferable. Currently, in the market, one can find fenestrated and branched stent-grafts [3]; these devices are suitable to treat aneurysms that involve peripheral arteries in order to maintain the blood flow.

In stent-grafts with sinusoidal stents, the number of apexes influences the sealing: the higher the number of apexes, the higher the number of points that press the graft onto the artery providing superior sealing. Biocompatibility, i.e., the ability of a material to remain biologically innocuous during its functional period inside a living creature [4], is of decisive importance since stent-grafts are placed inside the human body in direct contact with blood. Hence, the materials chosen, besides being biostable, cannot be toxic, allergic or carcinogenic; they also cannot cause thrombosis and hemolysis. It is desirable that they promote a thin hyperplasia, but the human body must tolerate them so as not to cause a foreign body reaction or an inflammatory reaction. Furthermore, the

device should be capable of being adequately sterilized and stored as an "off-the shelf" product. The “ideal” stent-graft should have and maintain the same compliance as a normal aorta without interfering with the surrounding anatomical structures. Additionally, its design ought to be the least invasive possible and be able to conform to the aorta’s anatomy in order to minimize flow resistance and pressure drops. In fact, the best stent-graft will be the one that can overcome most of the anatomical obstacles, thus achieving success in the largest number of cases. Stent-grafts should also mimic the aorta’s mechanical properties. Not only should they exceed the patient’s life expectancy, but they also should be flexible so that the profile can be maintained without kinking or bending. They should be tough yet ductile in order to avoid stent fracture and later complications. Furthermore, to withstand the continuous pulsatile blood flow, they should be fatigue resistant, wear resistant and have a stable configuration, i.e., they cannot allow excessive elongation, overexpansion or bursting. The rate of tissue in growth depends on the graft’s porosity [5] and it should be such that favors good healing and perfusion without being responsible for endoleaks or blood ultrafiltration. Radial force is another crucial feature in the design of a stent-graft. This force is important, not only for stents to stay open without being crushed with muscular activity, but also to provide a good seal and to ensure a secure fixation. When defining this parameter, it is necessary to make a trade-off: the device must be in its place without damaging the endothelium cells. In order to minimize stent-graft migration, currently, some devices have barbs; however, if the prosthesis fails, removing it is almost impossible due to the damages inflicted in the artery wall.

Radiopacity is an essential trait given that it is necessary to trace the stent-graft during the deployment and follow the evolution of the device within the patient's arteries.

Stent-grafts should have a low profile to facilitate the deployment and minimize lesions in the access arteries. From the selection point of view, a wide range of diameters and lengths is useful and, it is convenient if the materials used have a predictable behavior, that is, it is possible to foresee how much the device will dilate or shrink. Currently, after an EVAR, patients are regularly submitted to imaging exams to evaluate the size of the aneurysm sac and detect complications, such as endoleaks, endograft migration and module disconnection. The ideal stent-graft should be designed to avoid these expensive, and potentially harmful, exams; a possible solution is to include auto-diagnostic capabilities.

Regarding the device’s manufacture, besides being cost-effective, the processes adopted should be environmentally acceptable, in addition to assuring a high and consistent quality.

Some of the features listed above are “yes” or “no” answers, that is, if a material does not meet that requirement it is automatically excluded. However, others features, like the radial force, are difficult to define because trade-offs have to be made. In these cases, by building a house of quality would it is possible to determine the relations between the multiple requirements and find the most suitable value.

3. Multi-Plane Model

This multi-laminate model was initially proposed by Zienkiewicz, O.C., et al (1977)[6]. He suggested that the constitutive behavior of poly-crystal metals are explained by the relations between strain and tension vectors in planes with different orientations in which the macroscopic stress and strain tensors are obtained by sum of all the vectors in these planes using some static and kinematic constraints and formula. Many researchers have modified this method for alloys. Meanwhile, this method has been used for development of the non-linear hardening properties of other complex behavior materials such as geomaterials, soils and stones [7, 8, 9]. Multi-plane is referred to a plane in materials with different orientation which is used for estimation of the micro-structure behavior of materials. After extension of the multi-laminate model by Prat and Bazant (1988)[10] for estimation of damages arising from compression and tension, a very more effective formula for concrete was introduced by Bazant (2000)[11].

For each formula, in static and kinematic constraints, properties of material are identified by using stress and strain relations in multi-laminates. Induced anisotropy is generally, initiated and constructed during plastic shear deformation in materials and plays a key role in understanding the plastic behaviour of granular soil in a general stress state, including the rotation of principal stress axes (e.g. Sadrnejad, 1990) [12to15]. The observation and experiment on flow-type behaviour of liquefied soil has revealed that the influence of inherent fabric anisotropy on the residual strength of a granular soil is so drastic that the inherent anisotropy can no longer be ignored in sand modeling. The influence of fabric anisotropy is known since the emergence of the geo-mechanics (Sadrnejad, 2001) [16].

3.2 The Model Specifications

The multi-plane framework lies between macroscopic and microscopic scale. This method, investigate material behavior in several planes with different orientations which are called multi-plane. Each multi-plane can represent the multi-structure behavior of one orientation of one point of material.

In this method we can study more simply the multi-structural behavior in form of relation between on plane stress and deformation vectors instead of macro-scale relationship between stress-strain tensors or their invariants. For this purpose we must first select some multi-planes and their orientations for one point of material. The number of selected planes depends on behavior of material and precious of our numerical integration. Then by transferring the stress tensor or strain tensor on each multi-plane we obtain the planar stress or strain vector in the case of static or kinetic constraint method respectively.

Multi-laminate or multi-laminate framework by defining the small continuum structural units as an assemblage of material particles and voids that fill infinite spaces between

the sampling planes, has appropriately justified the contribution of interconnection forces in overall macro-mechanics. Upon these assumptions, thermo-plastic deformations are to occur due to sliding, separation/closing of the boundaries and elastic deformations are the overall responses of structural unit bodies. Therefore, the overall deformation of any small part of the medium is composed of total elastic response and an appropriate summation of sliding, separation/closing phenomenon under the current effective normal and shear stresses/strains on sampling planes.

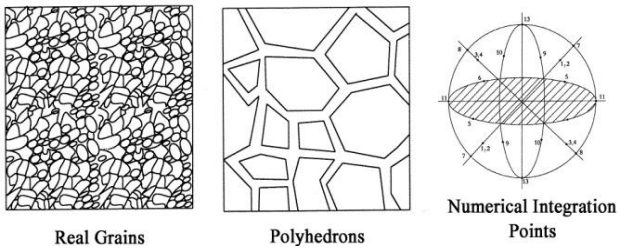

Fig.1: grains, assumed polyhedrons, sampling points

Direction Cosines			Weight	Direction cosins			Weight
ℓ_i	m_i	n_i	W_i	ℓ_i	m_i	n_i	W_i
$\sqrt{1/3}$	$\sqrt{1/3}$	$\sqrt{1/3}$	27/840	$\sqrt{1/3}$	$-\sqrt{1/3}$	$\sqrt{1/3}$	27/840
$-\sqrt{1/3}$	$\sqrt{1/3}$	$\sqrt{1/3}$	27/840	$-\sqrt{1/3}$	$-\sqrt{1/3}$	$\sqrt{1/3}$	27/840
$\sqrt{1/2}$	$\sqrt{1/2}$	0.0	32/840	$-\sqrt{1/2}$	$\sqrt{1/2}$	0.0	32/840
$\sqrt{1/2}$	0.0	$\sqrt{1/2}$	32/840	$-\sqrt{1/2}$	0.0	$\sqrt{1/2}$	32/840
0.0	$-\sqrt{1/2}$	$\sqrt{1/2}$	32/840	0.0	$+\sqrt{1/2}$	$\sqrt{1/2}$	32/840
1.0	0.0	0.0	40/840	0.0	1.0	0.0	40/840
0.0	0.0	1.0	40/840				

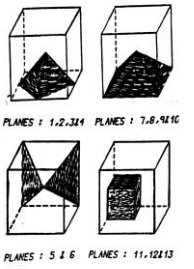

Fig.2: Direction cosines, weighted coefficient, sampling planes

These assumptions adopt overall sliding, separation/closing of inter-substructure points of particles included in one structural unit are summed up and contributed as the result of sliding, separation/closing surrounding boundary planes. This simply implies thermal deformation, yielding/failure or even ill-conditioning and bifurcation response to be possible over any of the randomly oriented sampling planes. Consequently, thermo-plasticity control such as yielding should be checked at each of the planes and those of the planes that are sliding will contribute to cycles of plastic deformation. Therefore, any of the solid material mass has an infinite number of yield functions usually one for each of the planes in the physical space.

Figure1 shows the arrangement of artificial polyhedron simulated by real solid material. The created polyhedrons are roughly by 13 sliding planes, passing through each point in medium. The location of tip heads of normal to the planes defining corresponding direction cosines are shown on the surface of unit radius sphere (Figure 2).

In this paper the static constraint method with 26 different planes is used.

For obtaining shear strains and their orientations in each multi-plane, it is required that a constitutive law to be defined in each multi-plane. In this model a 2-D thermo-mechanic phase transformation surface for each plane has been defined. The 2-D phase transformation surfaces in each plane are dependent on the in plane shear component direction and the plane orientation and the stress tensor path.

In shape memory alloys , overall martensite strain of one polycrystal point of materials is the sum of martensite shear deformation in the planes with different orientation related to the each single crystal in that point.

Below considerations have been assumed for facilitating the development of the model:

- Negligibility of thermal expansion
- Elasticity of volumetric strain

The constitutive law used for each multi-plane, in this model, has been obtained by modification of the one-dimensional constitutive law presented by Amir Sadjadpour and Kaushik Bhattacharya. This constitutive law has been obtained using thermo-dynamics relations presented in [17].

3-3 Multi-Plane Model Based on Static Constraint

In this method the stress components in the k_{th} multi-plane are obtained by transforming of the macro-scale stress tensor of σ_{ij} in the k_{th} multi-plane (Fig. 3). So, first the strain components of each plane are obtained using the constitutive law of that multi-plane and then the macro-scale strain tensor is obtained using the virtual work principle [17].

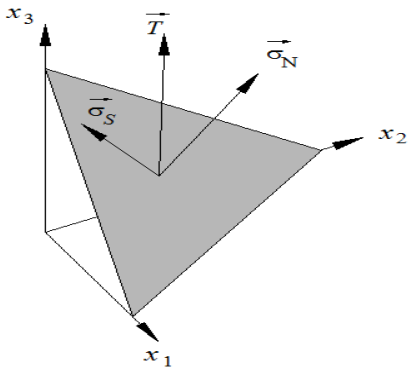

Fig.3: the components of stress tensor on multi-laminate

Stress components could be obtained as below:

$$T_i^{\,k} = \sigma_{ij}\, n_j^{\,k} \quad i,j = 1,2,3 \tag{1}$$

$$\sigma_N^{\,k} = \sigma_{ij} n_i^{\,k} n_j^{\,k} \tag{2}$$

$$\sigma_s^{\,k} = \sigma_{ij}\left(\frac{s_i^{\,k} n_j^{\,k} + n_i^{\,k} s_j^{\,k}}{2}\right) \tag{3}$$

$$s_i^{\,k} = \frac{T_i^{\,k} - \sigma_N^{\,k}\, n_i^{\,k}}{\sigma_s^{\,k}} \tag{4}$$

$T_i^{\,k}$ is the i_{th} component of stress tensor and $n_i^{\,k}$ is the i_{th} component of unit normal vector and $\sigma_N^{\,k}$ is the vertical component of stress tensor and $\sigma_s^{\,k}$ is shear component of stress tensor, all in the k_{th} multi-plane.

The vertical component ${\sigma_N}^k$ could be divided in deviatoric term ${\sigma_D}^k$ and volumetric term ${\sigma_V}^k$ in the k_{th} multi-plane as below:

$${\sigma_V}^k = \frac{\sigma_{ii}}{3} = \sigma_{ij} \times \frac{\delta_{ij}}{3} \quad (5)$$

$${\sigma_D}^k = {\sigma_N}^k - \frac{\sigma_{ii}}{3} \quad (6)$$

Based on the virtual work principle:

$$\varepsilon_{ij} = \frac{3}{4\pi}\int_\Gamma \left[{\varepsilon_v}^k\left(\frac{1}{3}\delta_{ij}\right) + {\varepsilon_D}^k\left({n_i}^k{n_j}^k - \frac{1}{3}\delta_{ij}\right) + \frac{{\varepsilon_s}^k}{2}\left({s_i}^k{n_j}^k + {n_i}^k{s_j}^k\right)\right] d\Gamma \quad (7)$$

Γ is the surface of the unit hemisphere. Equation (7) has been derived based on the fact that the virtual work inside the hemisphere and external surface is equal. Integral of the equation (7) can be derived using numerical methods of Gaussian integral with a series of points over the surface of the hemisphere. In other words, we can simulate the integral over surface of hemisphere (right hand of equation 7) by closed poly surfaces which inner volume is equal to unit hemisphere. This method uses a limited series of multi-planes with different orientations for every point.

4. Constitutive Law on Multi-Plane

Suppose a point of these materials which consist of a number of grains. Each grain includes several austenite and martensite multi-structures and each martensite multi-structure consists of variants of martensite with different orientations.

The kinematic of multi-structure could be represented by two parameters $\lambda(x,t)$ named *volume fracture factor* and $\varepsilon_m(x,t)$ named *the martensite strain tensor* for point *x* in time *t*.

The volume fracture factor is equal to the volume of martensite multi-structure divided by total volume of that point of material which lie between two scalar values 0 and 1. The value of 0 is related to the full austenite and the value of 1 represents the full martensite multi-structure of one point of material.

The martensite strain tensor $\varepsilon_m(x,t)$ could be obtained by multi-plane method in equation (8) and (9). This tensor include of two important distinctions: the direction of the unit martensite strain tensor $E_{m_{ij}}$ and the scalar magnitude of the martensite strain tensor $\bar{\varepsilon}_m$. The unit martensite strain tensor $E_{m_{ij}}$ obtains by normalizing the martensite strain tensor $\dot{E}_{m_{ij}}$ from (10) and the martensite strain tensor $\dot{E}_{m_{ij}}$ derives by super posing the on plane shear strains from (11) with considering only the shear component of on plane strains in virtual work equation (7).

$$\dot{\varepsilon}_{m_{ij}} = \dot{\lambda}\bar{\varepsilon}_m E_{m_{ij}} \quad (8)$$

$$\varepsilon_{m_{ij}} = \lambda\bar{\varepsilon}_m E_{m_{ij}} \quad (9)$$

$$E_{m_{ij}} = \frac{\dot{E}_{m_{ij}}}{\sqrt{\dot{E}_{m_{ij}} : \dot{E}_{m_{ij}}}} \quad (10)$$

$$\dot{E}_{m_{ij}} = \sum_{k=1}^{13} W_k \lambda_p^k F(k)_p \times \frac{1}{2}\left(s_i^k n_j^k + n_i^k s_j^k\right) \quad (11)$$

$F(k)_p$ in eq. (11) is the on plane proportion factor which could be obtained by eq. (12).

$$F(k)_p = \Sigma_{ij} s_i^k n_j^k \quad (12)$$

Σ_{ij} in eq. (12) is the unit stress tensor:

$$\Sigma_{ij} = \frac{1}{s}\sigma_{ij} \quad , \qquad s = \sqrt{\sigma_{ij} : \sigma_{ij}} \quad (13)$$

It must be mentioned that in equation (11), the direction of the martensite strain tensor is derived by principle of the virtual work without considering of two items relevant to the volumetric term ${\varepsilon_v}^k$ and deviatoric term ${\varepsilon_D}^k$ of the vertical component of strain vector on multi-planes. The reason is that since the martensite strain tensor is self accommodate multi structure, it is a trace free or deviator tensor. So the volumetric terms ${\varepsilon_v}^k$ are zero on all multi-planes. Also, it could be proved that when the martensite strain tensor is a deviator tensor, the direction of strain tensor derived from the normal deviatoric term ${\varepsilon_D}^k$ and the shear component ${\varepsilon_s}^k$ of on plane strain vectors in equation (7) are the same and proportion. So for calculating the direction of the martensite strain tensor, it is enough that we just consider the shear component of strain vector ${\varepsilon_s}^k$ on multi-planes as could be seen in equation (11).

It is obvious that the martensite strain tensor under every stress path, reaches to maximum value when the volumetric fracture factor λ reaches to 1 when the multi-structure of the point become martensite completely (equation (14)).

$$\varepsilon_{m_{ij}(\max)} = \bar{\varepsilon}_m E_{m_{ij}} \quad (14)$$

The martensite strain tensors is a symmetric and trace free tensor so it has five independent components that lives in a five dimensional symmetry- trace free sub-pace. Suppose the set *P* is a five dimensional sub-space that the martensite strain tensor growth interior it with deformation rapidly until reaches on boundary ∂P.

We define the set *P* as below:

$$\varepsilon_{m_{ij}} \epsilon P \ , \ P = \{\varepsilon_m | tr(\varepsilon_m) = 0, g(\varepsilon_m) \leq 0\} \quad (15)$$

g is a function as below:

$$g: R_{dev}^{3\times 3} \longrightarrow R \quad (16)$$

In an isotropic phase transformation for every rotational vector *R*, we can say:

$$g(\varepsilon_m) = (R^T \varepsilon_m R) \quad (17)$$

It implies that we can define the martensite strain function $g(\varepsilon_m)$ by three invariant of the martensite strain tensor as below:

$$I_1(\varepsilon_m) = tr(\varepsilon_m) = 0$$
$$I_2(\varepsilon_m) = \frac{1}{2}[tr(\varepsilon_m^2) - tr(\varepsilon_m^2)] = -\frac{1}{2} \times tr(\varepsilon_m^2)$$
$$I_3(\varepsilon_m) = det(\varepsilon_m) \quad (18)$$

For an alloy with asymmetry response in tension and compression, we can define the set *P* as below:

$$g(\varepsilon_m) = g\big(I_2(\varepsilon_m), I_3(\varepsilon_m)\big) \quad (19)$$
$$P = \left\{\varepsilon_m \middle| tr(\varepsilon_m) = 0, g(\varepsilon_m) = (-I_2(\varepsilon_m))^{\frac{3}{2}} - aI_3(\varepsilon_m) - b \le 0\right\} \quad (20)$$

a, b could be obtained if we have the maximum values of martensite strain tensor ε_m on the boundary of ∂P for two different stress path. If we have two parameter a and b , Then we can determine the total set of *P* and it's boundary ∂P. Then we can have the maximum values of magnitude of martensite strain tensor $\bar{\varepsilon}_m$ which could be taken place for every stress path. For this we first must obtain Σ_{ij} and $F(k)_P$ and $E_{m_{ij}}$from equations (10) to (13), then with considering the volume fracture factor λ equal to 1, get the invariants $I_2(\varepsilon_m), I_3(\varepsilon_m)$ based on the $\bar{\varepsilon}_m$ from equations (18) and finally, we calculate the value of $\bar{\varepsilon}_m$ by substituting $I_2(\varepsilon_m), I_3(\varepsilon_m)$ in to the equation (19). The boundary of function g for various value of a and b are presented in principle strain coordinate system in Figure 4. As it could be seen, parameter a determines the intensity of asymmetry response in tension and compression and parameter b determines the magnitude of boundary surface of function g.

Having the increment of volume fracture factor $\dot{\lambda}$ for every increment of stress and the value of maximum magnitude of martensite strain $\bar{\varepsilon}_m$ for stress path, the increment of strain tensor could be obtained for placement x at timet_i:

$$\dot{\varepsilon}(x, t_i) = \dot{\varepsilon}_e(x, t_i) + \dot{\varepsilon}_m(x, t_i) \quad (21)$$
$$\varepsilon_m(x, t_i) = \lambda(x, t_i)\bar{\varepsilon}_m(x, t_i)E_m(x, t_i) \quad (22)$$
$$\dot{\varepsilon}_m(x, t_i) = \varepsilon_m(x, t_i) - \varepsilon_m(x, t_{i-1}) \quad (23)$$

The on plane constitutive law used for multi-plane model, which relates shear strain to shear stress in multi-planes, obtained within continuum thermo dynamic framework developed by sadjadpour [19]. The mentioned constitutive law relations in macro scale are as following:

$$\sigma = D(\varepsilon - \lambda\bar{\varepsilon}_m E_m) \quad (24)$$
$$\eta = \lambda\frac{\mathcal{L}}{\theta_{cr}} - c_p\left(1 + ln\left(\frac{\theta}{\theta_0}\right)\right) \quad (25)$$
$$\omega(\theta) = \frac{\mathcal{L}}{\theta_{cr}}(\theta - \theta_{cr}) \quad (26)$$
$$d_\lambda = \sigma : \varepsilon_m - \omega(\theta) \quad (27)$$
$$d_{\varepsilon_m} = \lambda\sigma \quad (28)$$

In the above equations D is elastic modulus matrix, ε is the total strain tensor, η is the entropy density, $\mathcal{L}$ is the latent heat of transformation, θ_{cr} is the thermodynamic transformation temperature , c_p is the heat capacity (assumed to be equal in both the austenite and martensite), θ_0 is the initial temperature, θ is the current temperature, $\omega(\theta)$ is the difference of chemical energy between austenite and martensite phases, d_λ is the driving force associated with the volumetric fraction, d_{ε_m} is the driving force associated with the martensite strain.
Equation (27) implies that the phase transformation from austenite to martensite in free stress state starts when:

$$d_\lambda^+ = -\omega(M_s) \quad (29)$$

Also, reverse phase transformation in free stress state happens when:

$$d_\lambda^- = -\omega(A_s) \quad (30)$$

In the above equations, A_s and M_s are the temperatures in which the transformation to austenite and martensite phase are started when the external tension is zero.
Hence, in macro scale, the stress induced phase transformation and reverse phase transformation occur when we reach the conditions below respectively:

$$d_\lambda = \sigma : \varepsilon_m - \omega(\theta) \ge d_\lambda^+ \quad (31)$$
$$d_\lambda = \sigma : \varepsilon_m - \omega(\theta) \le d_\lambda^- \quad (32)$$

In multi-plane scale, although, the conditions above are revolved to the following equations:

$$\sigma_s{}^k . \bar{\varepsilon}_m{}^K \ge (d_\lambda^+ + \omega(\theta)) \times \frac{(\Sigma_{ij} s_i^K n_j^K)^2}{\Sigma_{ij} E_{ij}} \quad (33)$$

$$\sigma_s{}^k . \bar{\varepsilon}_m{}^K \ge (d_\lambda^- + \omega(\theta)) \times \frac{(\Sigma_{ij} s_i^K n_j^K)^2}{\Sigma_{ij} E_{ij}} \quad (34)$$

Equations (33) and (34) could be obtained by establishing the energy balance law inner and outer the supposed unit hemisphere when the phase transformation or reverse phase transformation starts.

The energy balance law in thermodynamic, results the relation of temperature evolution for adiabatic condition:

$$\theta(t) = \theta_0 \, exp\left(\frac{(\lambda(t)-\lambda_0)\mathcal{L}}{c_p \theta_{cr}}\right) \tag{35}$$

The kinetic relation describes the evolution of martensite volume fraction in each multi-laminate. We define it for time step *i*, by modifying the mathematical function used by sadjadpour [21] as following:

$$\dot{\lambda} = \begin{cases} \dot{\lambda}^{+}\left(\frac{\Delta d_{\lambda_i}}{\Delta d_{\lambda_{i-1}}}\right)\left(1+(d_\lambda - d_\lambda^{+})^{-1}\right)^{\frac{-1}{p}} & d_\lambda > d_\lambda^{+} \\ \dot{\lambda}^{-}\left(\frac{\Delta d_{\lambda_i}}{\Delta d_{\lambda_{i-1}}}\right)\left(1+(d_\lambda^{-} - d_\lambda)^{-1}\right)^{\frac{-1}{p}} & d_\lambda < d_\lambda^{-} \\ 0 & Other\ wise \end{cases} \tag{36}$$

$\dot{\lambda}^{+}$ and $\dot{\lambda}^{-}$ and p are the kinetic parameters that obtain by calibrating with experimental data.

Parameters $\dot{\lambda}^{+}$ and $\dot{\lambda}^{-}$ determine the slope of the loop in stress-strain curve in loading and unloading path respectively. Δd_{λ_i} and $\Delta d_{\lambda_{i-1}}$ are the increment of deriving force of martensite volume fracture in time step *i* and (*i-1)* respectively.

This kinetic law can represent the inherent loading rate effect behavior of these materials [21].

Another phenomenon that can affect the loading rate effect behavior in these materials is the evolution of temperature in adiabatic condition during phase transformation. The developed model can represent it with considering the effect of increasing of temperature during phase transformation from equations (26) and (27).

In each sampling plane the relations to calculate modulus matrix C_{6x6} are as follows:

$$\tilde{\sigma}^{k}_{3\times1} = \begin{Bmatrix} \sigma_V^k \\ \sigma_D^k \\ \sigma_s^k \end{Bmatrix} = {T^k_{6\times3}}^{T} \times \tilde{\sigma}_{6\times1} \tag{37}$$

$$T^k{}_{6\times3} = \begin{bmatrix} \frac{1}{3} & (n_1^k)^2 - \frac{1}{3} & s_1^k n_1^k \\ \frac{1}{3} & (n_2^k)^2 - \frac{1}{3} & s_2^k n_2^k \\ \frac{1}{3} & (n_3^k)^2 - \frac{1}{3} & s_3^k n_3^k \\ 0 & 2n_1^k n_2^k & s_1^k n_2^k + n_1^k s_2^k \\ 0 & 2n_2^k n_3^k & s_2^k n_3^k + n_2^k s_3^k \\ 0 & 2n_1^k n_3^k & s_1^k n_3^k + n_1^k s_3^k \end{bmatrix}_{6\times3} \tag{38}$$

$$\varepsilon^{k}_{3\times1} = C^{k}_{3\times3}\sigma^{k}_{3\times1} \tag{39}$$

$$C^{k}_{3\times3} = C^{k}_{e_{3\times3}} + C^{k}_{m_{3\times3}} \tag{40}$$

$$C^{k}_{e_{3\times3}} = \frac{1}{E}\begin{bmatrix} 1-2\nu & 0 & 0 \\ 0 & 1+\nu & 0 \\ 0 & 0 & 1+\nu \end{bmatrix} \tag{41}$$

$$C^{k}_{m_{3\times3}} = \begin{bmatrix} 0 & 0 & 0 \\ 0 & 0 & 0 \\ 0 & 0 & \frac{\varepsilon_m^{k\ i+1}}{\sigma_s^k} \end{bmatrix} \tag{42}$$

$$\varepsilon^{k}_{3\times1} = C^{k}_{3\times3}\sigma^{k}_{3\times1} \tag{43}$$

Substituting the above equations to equation (7):

$$\tilde{\varepsilon}_{6\times1} = \left(6 \times \sum_{k=1}^{13} W_k T^k_{6\times3} C^k_{3\times3} {T^k_{6\times3}}^{T}\right)\tilde{\sigma}_{6\times1} \tag{44}$$

$$C_{6\times6} = 6 \times \sum_{k=1}^{13} W_k \, T^k_{6\times3} C^k_{3\times3} {T^k_{6\times3}}^{T} \tag{45}$$

W_k is the weighted coefficient related to k^{th} plane which are proportion with the area of each plane.

5. Current Materials

Since Parodi´s stentgraft, these devices have not known significant changes regarding both the configuration and the materials used.

Nitinol, an acronym for NiTi Naval Ordnance Laboratory, is an alloy composed of nickel (Ni) – between 49.5% and 57.5% - and balance titanium (Ti). In biomedical applications, the 55-Nitinol (55 weight% Ni) is the most common due to its shape memory properties that allow the creation of complex shapes and its ductility at low temperatures [22].

Super elasticity and the shape memory effect are two of the most prominent features of these alloys. Both characteristics derive from a solid-state transformation, from martensitic to austenitic, which can be triggered thermally or mechanically, and are dependent on the composition and processing history of the material [22].

Super-elastic Nitinol exhibits a hysteretic stress-strain relationship similar to the behavior of natural materials. This feature, which usually is regarded as a drawback in traditional engineering applications, is useful in the design of stent-grafts because it is responsible for a constant force against the organ wall and resistance to crushing. Along with the shape memory effect, super elasticity is important during the device's deployment to help the stent-graft acquire its final shape. In addition, both properties are crucial to resist kinking or, more suitably, recover from crushing [23].

Regarding Nitinol's fatigue resistance, literature indicates lower endurance values when compared with those of others metals used as stent structures (e.g., stainless steel and Elgiloy). However, this subject is still under research with limited information available. While the quasi-static tension and compression properties of Nitinol are reasonably well characterized, its fatigue behavior is not. Nitinol strength is widely influenced by the mechanical cycling and by the effect of cycling temperature [24]. Furthermore, the non-linear nature of the super elastic phase transformation in Nitinol means that conventional fatigue life theory is difficult to apply. The

volume fraction of martensitic/austenitic phases and its role in the fatigue mechanism is still not clearly understood [25]. Many additional factors can affect the fatigue behavior of Nitinol alloys, like microstructure, surface quality, and type of loading, degree of order of the lattices and particles size distributions [26].

Nickel is known to be allergenic and toxic; however, Nitinol is biocompatible and, to improve its biocompatibility and corrosion resistance; studies are being carried out to eliminate Ni from the surface [27].

Nitinol is self-passivating, that is, it forms a stable oxide surface layer that protects the base material from general corrosion. Literature shows that the titanium-oxide layer formed remains essentially unchanged after implantation but samples from surrounding tissues from the vascular wall around Nitinol stents has revealed tiny deposits of nickel and titanium compounds, which means that corrosion products have been formed and certainly have diffused through the passive layer, thus reaching surrounding tissues [28]. To prevent this from happening, passivation treatments, such as electro-polishing or chemical passivation, are needed. These techniques contribute to the elimination of many surface irregularities that are the starting point for stress fractures or erosive pits and increase the stability of the surface by protecting the bulk material from corrosion, thus increasing the device's durability [29].

5.1. Materials for Stents

Stent-grafts can be either balloon-expandable or self-expanding. While the formers are manufactured in the deliverable configuration, and balloon-dilated to the final diameter inside the vessel, self-expanding stent-grafts are manufactured in the expanded shape, compressed and constrained in a delivery system, and, upon release, spring back to the preset diameter.

The materials used for balloon-expandable devices (notice that these devices are rare) are plastically deformed through the inflation of a balloon and, after the balloon is deflated, suffer slight recoil caused by the elastic portion of the deformation. Therefore, the ideal material for these devices should have low yield stress, to make it deformable at manageable balloon pressures, and high elastic modulus for minimal recoil. In addition to the mechanical behavior, they should have enhanced radiopacity, good corrosion resistance and good MRI compatibility. Possible materials for these types of stents are tantalum, platinum alloys, Niobium alloys and Cobalt alloys [38-40]. During the design of stent-grafts, attention must be given to galvanic corrosion. Thus, the use of multiple alloys should be avoided.

We now demonstrate the model by calculating the response of a material point to a given applied stress history $\sigma_{11} = A\sin\omega t$, and then conduct a parameter study and present capability of model:

According to the studies on a type of NiTi alloy conducted by Mc Naney et al., parameters of material can be considered as follows:

$$M_s = -51.55^\circ C \quad A_s = -6.36^\circ C \quad \ell = 12.3(J/gr)$$
$$C_p = 837 J/kg^\circ k \quad \varepsilon_c^m = -2.5\% \qquad \varepsilon_t^m = 5\%$$
$$E = 65GPa \qquad \sigma_y = 1500MPa$$

Using equations 10, 22 and 23, the below relations are obtained:

$$d\lambda^+ = f(a)\ell\left(\frac{Ms - As}{As + Ms}\right) d\lambda^- = g(a)\ell\left(\frac{As - Ms}{As + Ms}\right) \tag{27}$$

$$\theta_{cr} = \frac{As + Ms}{2} \tag{28}$$

Now, with regard to the single axis tension as $\sigma_{11} = A\sin\omega t$ in which $A = 1300\ MPa$ and, $\omega = 2\pi/T$ and $T = 5\times10^{-3}$ sec, the initial conditions are as follows:

$$\varepsilon(0) = 0 \qquad \varepsilon_p(0) = 0 \qquad \varepsilon_m(0) = 0$$
$$\lambda(0) = 0 \qquad \theta(0) = 0$$

After comparing the results with the experimental results given by Mc Naney [31], the parameters obtained for the material are as follows:

$$a = 0, \quad \alpha = 5.65, \quad f(0) = 1 \quad , \quad P = 2,$$
$$g(0) = -0.4 \quad , \quad H = E/50, \quad \dot{\lambda}^+ = -\dot{\lambda}^- = 0.1$$

It should be mentioned of $A < \sigma_y$, so we will not enter the plastic strain limits. The responses resulted from multi-laminate model have been shown in the Figure 4-a.

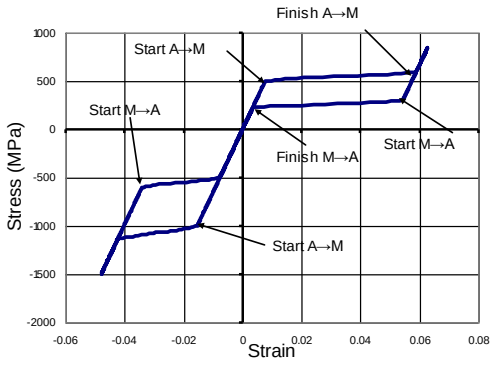

Fig. 4-a: A typical curve of stress-strain obtained from the multi-laminate model during a harmonic loading cycle

It can be seen that loading is started in a elastic state until it reaches the northwest point in the upper loop. Here, the phase transformation from austenite to martensite begins, so the slope of the curve is changed. Then, it reaches the north east point in the upper loop in which the phase transformation is completed and reaches the phase of martensite completely. Again by increase of the load, it returns to the elastic state and the slope of the cure reaches the initial slope.

In the unloading path, the curve returns with this slope until it reaches to the southeast point. Here, the martensite phase begins to change to austenite phase. Continuing

unloading the material is completely turned into austenite phase and it reaches to south west point in the upper loop. Then it reaches again in linear-elastic term until the tension and strain reaches zero. Similarly, for the compression loading, a loop is formed, but the tensile loop is a little different from compression loop. This phenomenon proves the asymmetry in tension and compression of alloys which can be seen in this model.

Figure 4-b shows a comparison between uniaxial stress and strain which has been derived from the experimental studies conducted by Mc Naney and the curve obtained from multi-laminate model.

Parameters of materials are as the same of the abovementioned ones, except for $E = 40\ GPa$ and $\ell = 8.3(J/gr)$.

It can be clearly seen that all the curves are coincide, only slope of curves in the reverse path is a little different in the linear-elastic term, this is due to the fact that in this model it has assumed that the elasticity module is constant in both austenite and martensite phase. It can be changed easily.

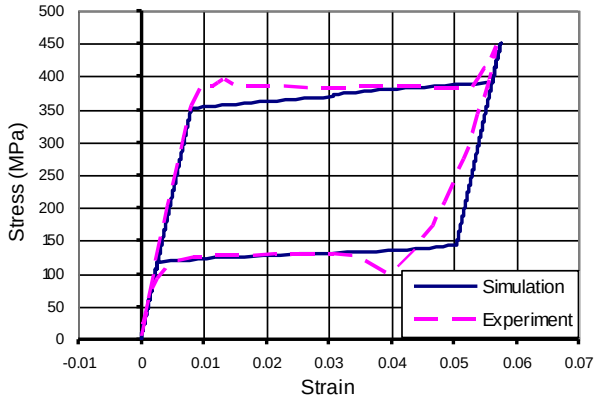

Fig 4-b: Comparison between multi-laminate model and experimental data obtained by Mc Naney et al. [31] as the result of uniaxial loading and unloading.

5.1. Loading Rate

Figure 5 shows the uniaxial stress-strain curve with loading and unloading cycles with different rates. As it can be seen, the starting point of phase transformation does not change with increase of stress rate. But because the stress rate is more than martensite strains rate, a hardening occurs in these curves and so an increase in the surface of loops is seen.

Also, in the curve related to the highest rate of loading, a residual strain can be seen because the unloading rate is so high that before the austenite phase is completed and strains related to phase transformation reach zero, unloading is completed and tension reaches zero. These all is related to stick-slip behavior. Also, in the curve related to the highest rate of loading, a softening can be seen because the loading rate is so high that before phase transformation is finished, loading reaches to pick of sinus cycle and so when unloading started, phase transformation still continues. All these results comply with experimental results [31].

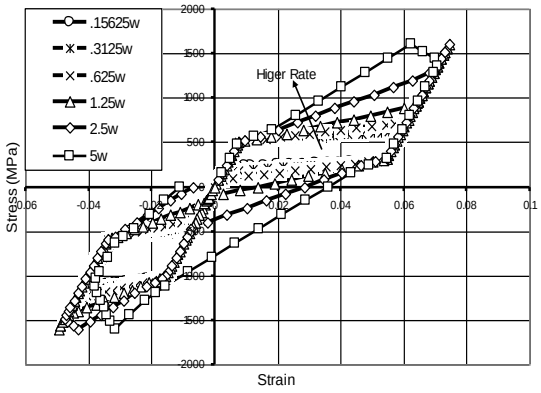

Fig 5: Numerical results related to single axis tension-strain with different rates of harmonic loading and unloading

5.2. Ambient Temperature and Investigating the Shape Memory Effect

Figure 6 shows the temperature variations (-70, -40, -10, 20, 50, 70, 110, 140, 170, respectively) effects in stress-strain curves. In this case, different environment temperatures have been assumed as the initial temperature θ_0 and the same harmonic uniaxial loading has been applied.

As it can be seen, in the curve related to the least environment temperature i.e. -70C the coefficient λ increases sharply to the value of 1 in which the austenite phase has been turned into martensite phase, so it is independent to the loading and ε_m results from rotation of variant. By increase of environment temperature, for increase of the volumetric fraction coefficient λ, stress increasing is required till the environment temperature reached 170C and the phase transformation is not seen. All the results of this model comply with results from [32].

Also, by investigation of curves the shape memory effects can be perceived. As the temperature reduced to the value of -70C, the λ coefficient moves to reach 1 before loading but ε_m remains zero. In other words, reduction of temperature causes phase transformation without strain. If the stress increases a little, the strain of phase transformation increases rapidly and by unloading the residual strain remains.

However, if the environment temperature increases (say 20C) and then loading and unloading are carried out, no residual strain remains and as can be seen in the curve related to the temperature 20C, the stress related to the zero strain is zero which is the shape memory effect of alloys that can be seen in this behavioral constitutive law.

Figure 7 shows the numerical results of the multi-laminate model as the result of triangular uniaxial loading and unloading.

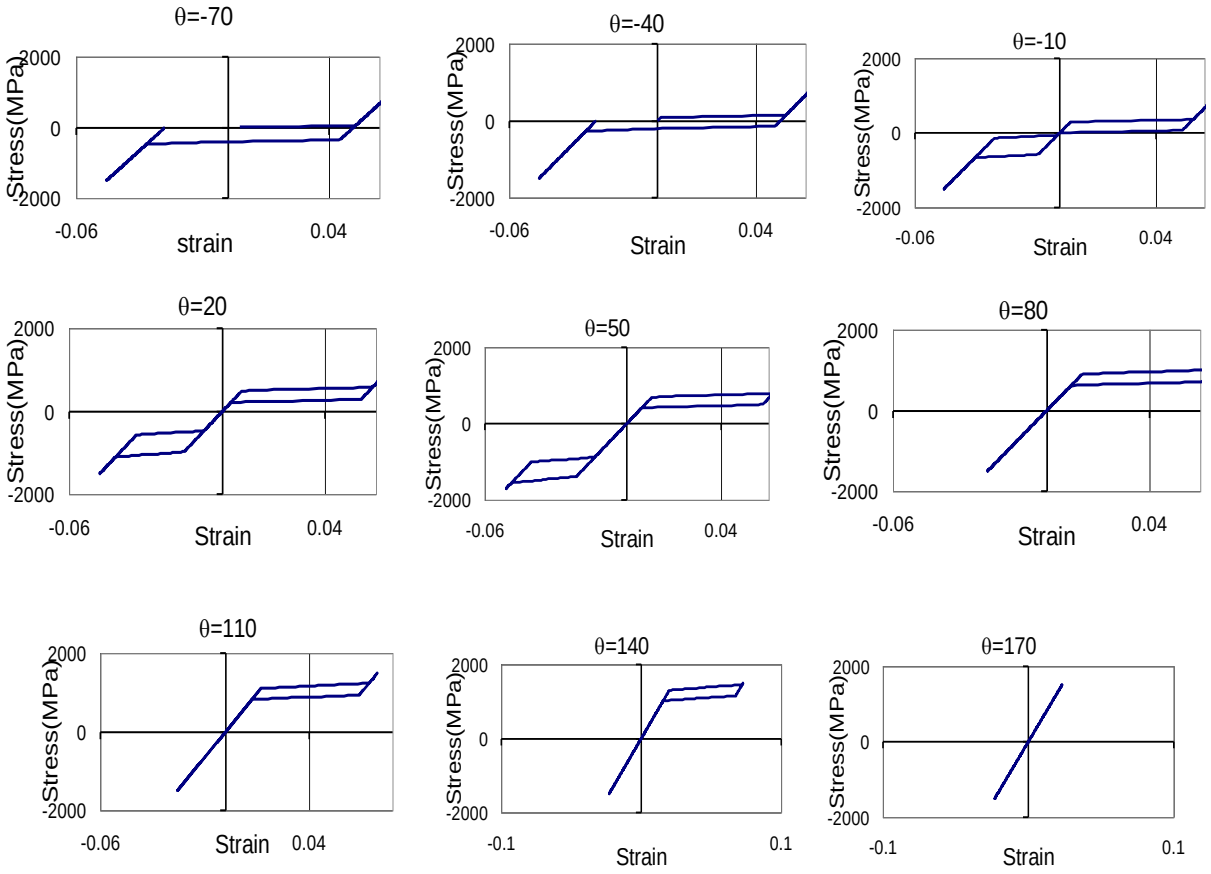

Fig 6: the numerical results of the effect of temperature changes on the single axis stress-strain curves

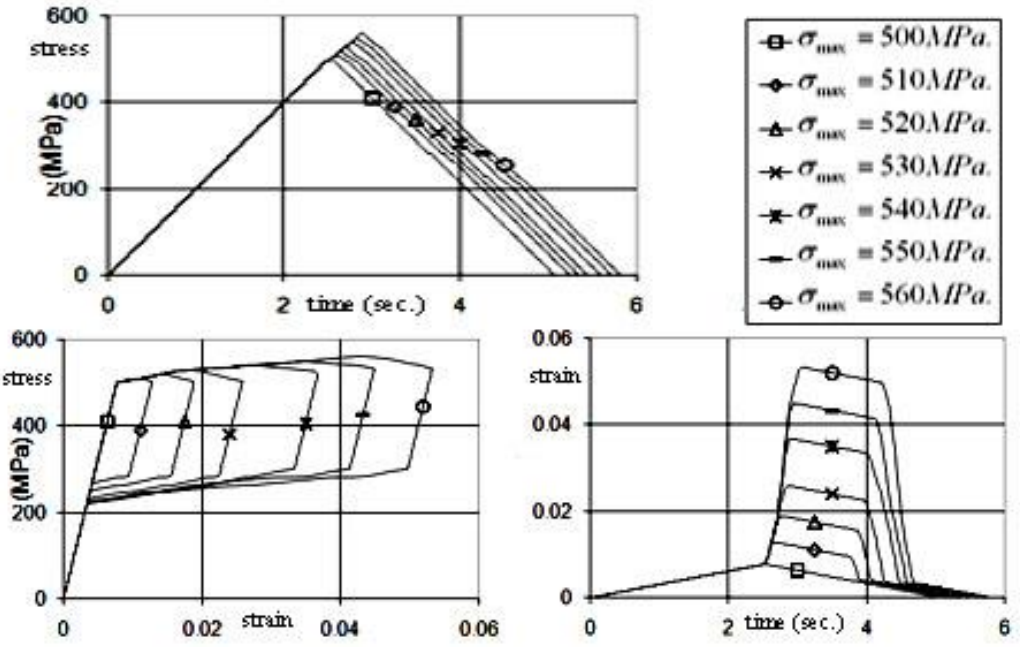

Fig 7: the numerical results of the multi-laminate model as due to triangular uniaxial loading and unloading

As it can be seen, in some of these curves, before completion of the phase transformations, unloading starts, so loops become smaller and return with the same slope until the reverse phase transformation starts and the strains of the phase transformation return to their initial state and the material turns to the austenite shape. In continuation, the material returns to the same state with zero stress and strain. These curves comply with the results stated by Abeyarante, Chu and James [33].

5.3. Effects of Hydrostatic Pressure

Although, the volumetric strains due to phase transformation have been neglected in this model, but small volumetric strains have been identified in nearly all of the experimental studies [34]. These volumetric strains cause behavior of these materials to be dependent on the hydrostatic stress [35]. This phenomenon can be seen by adding the normal effect of stress on the starting point of phase transformation in each multi-laminate:

$$d\lambda^{+} = f(a)\ell\left(\frac{Ms - As}{As + Ms}\right) + f'(a)\frac{\sigma_N^2}{E_I}$$
$$d\lambda^{-} = g(a)\ell\left(\frac{As - Ms}{As + Ms}\right) - g'(a)\frac{\sigma_N^2}{E_I} \qquad (29)$$

$f'(a)$ and $g'(a)$ are the functions relating to the normal stress and a is related to the shear stress path in the multi-laminate.

The comparison of the curves resulted by this method as shown in the Figure 8, the overall effect of the hydrostatic stress on the behavior of these materials can be seen. The curves are related to the effective stress $(\sigma_{11} - \sigma_{11}^{hyd})$ and effective strain $(\varepsilon_{11} - \frac{\varepsilon_v}{3})$ as the result of triangular loading and unloading of a material point in three cases. In the first case, without hydrostatic stress, loading as uniaxial tension stress and unloading to zero.

In the second case, first the point is under hydrostatic pressure of 50MPa and then the triangular shape uniaxial tension stress is loaded and unloaded. In the third case, the same work is done under the hydrostatic stress of 150MPa. In all the three cases, $f'(a)$ and $g'(a)$ have been considered 0.1 but these parameters can be obtained using experimental results.

As it can be seen, by increase of the hydrostatic stress, the materials starts to phase transformation in a higher tensile stress and the loop related to the phase shift moves upward. The obtained results comply with the behavior of these alloys qualitatively. [35]

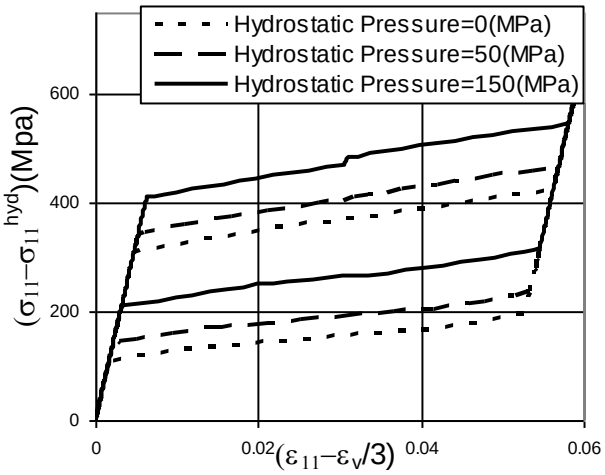

Fig 8: Effects of hydrostatic stress on the effective stress-effective strain curve obtained from multi-laminate model

5.4. Proportional Biaxial Loading

In this section, the results obtained from the model for a single point of the material which is under simultaneous loading and unloading stress σ_{11} and shear τ_{23} has been investigated in six different cases and compared with experimental results obtained by Mc Naney et al [31].
Six different cases of loading and unloading are as follows:

case1: Maximum tensile strain ε_{11} equals 6% and maximum shear strain (torsion) ε_{23} equals 0%

case2: Maximum tensile strain ε_{11} equals 6% and maximum shear strain (torsion) ε_{23} equals 2%

case3: Maximum tensile strain ε_{11} equals 3% and maximum shear strain (torsion) ε_{23} equals 2%

case4: Maximum tensile strain ε_{11} equals1.5% and maximum shear strain (torsion) ε_{23} equals 2%

case5: Maximum tensile strain ε_{11} equals 0.7% and maximum shear strain (torsion) ε_{23} equals 2%

case6: Maximum tensile strain ε_{11} equals 0% and maximum shear strain (torsion) ε_{23} equals 2%

After calibration of the model with experimental results obtained by Mc Naney et al the values for $d\lambda^{+}$ and $d\lambda^{-}$ in each multi-laminate can be introduced as a function of a based on equations (18) and (19) in which θ is the angles between the shear stress in each multi-laminate relative to the base direction. Here, the base direction is the direction of the shear stress resulting from the axis stress σ_{11} in it. The effects of these functions can be seen in the Figure 9.

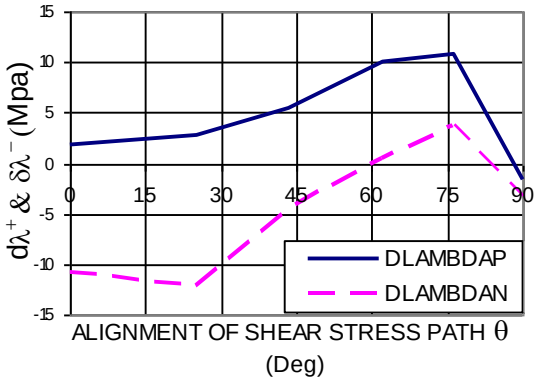

Fig 9: the changes of $d\lambda^+$ and $d\lambda^-$ relative to the angle θ

In Figure 10 the obtained results have been compared with the experimental results introduced by Mc Naney in the six loading and unloading paths. As it can be seen, the results nearly coincide with each other.

5.5. Non-proportional biaxial loading

The results obtained from the model for a single point of the material has been presented in case the point is under single axis stress in direction of σ_{11} and then shear stress is applied to it in the direction of τ_{23} as the stress σ_{11} remains constant, then shear stress unloading and tensile stress unloading is applied in three cases; The first case, the maximum tensile stress is equivalent to 0.7% of the axial strain and the shear stress is equivalent to 2% of the shear strain. In the second case, the Figures are 1.05% and 2% and in the third case the Figures are 6% and 2% respectively.

Figure 11 shows the results obtained from the multi-laminate model in comparison with the experimental results obtained by Mc Naney et al [31], first in net rotation case and then in the three mentioned loading cases.

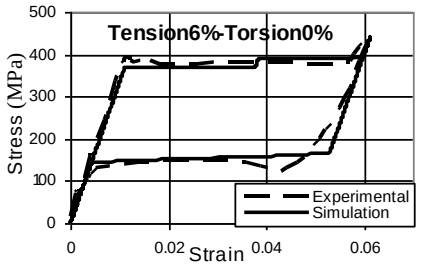

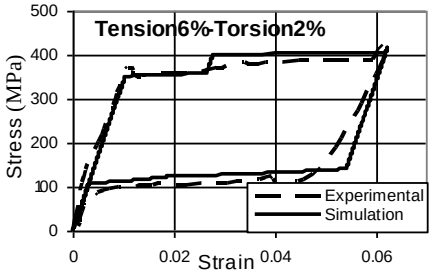

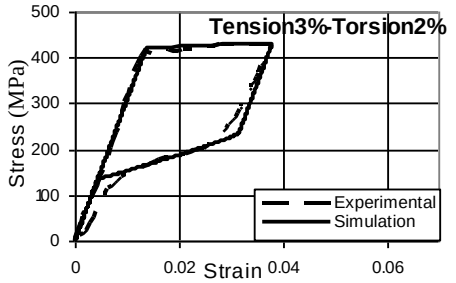

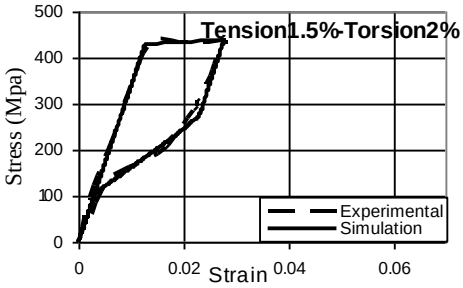

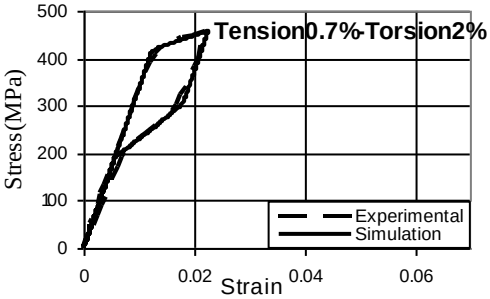

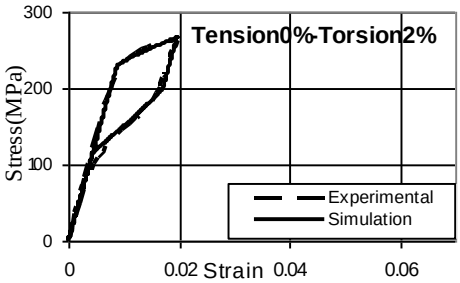

Fig 10: Comparison of the results obtained from multi-laminate model with the experimental results of Mc Naney in the six paths of biaxial tensile and rotational loading and unloading

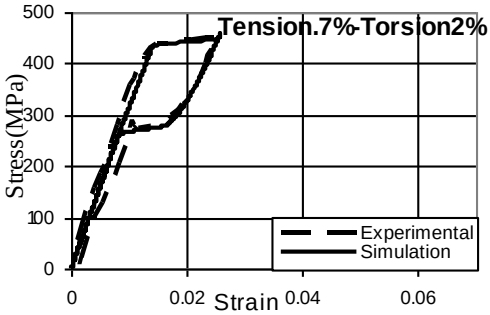

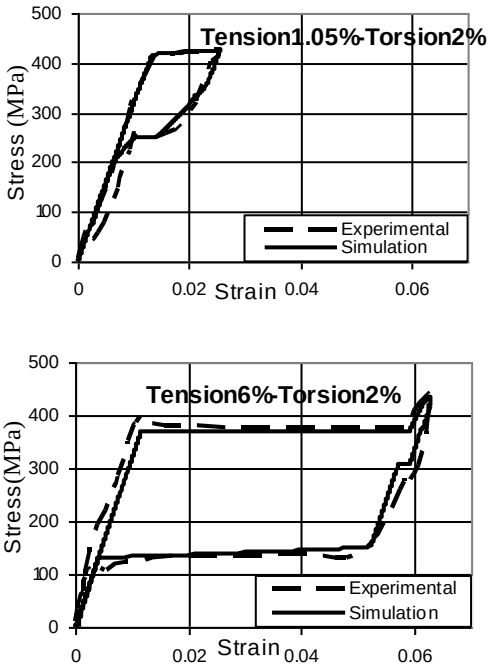

Fig.11: Comparison of the numerical results obtained from the multi-laminate model and the experimental results of Mc Naney et al for biaxial tensile and rotational loadings

6. Stent Analysis

A diamond shape stent as shown in Figure 12 that has been laser sheared a shape memory Nitinol, an acronym for NiTi, is an alloy composed of nickel (Ni) – between 49.5% and 57.5% - and balance titanium (Ti) pipe that analyzed by the proposed model. Upon the application of tensile stress exceeding nonlinearity level, phase change from austenite to martensite reduces the pipe radius into half to able entering artery. Removing tension and letting temperature to balance, changes the phase to austenite upon super elasticity and return the diameter to previous value. A light interaction pressure of artery and out surface of pipe created and kept it normal.

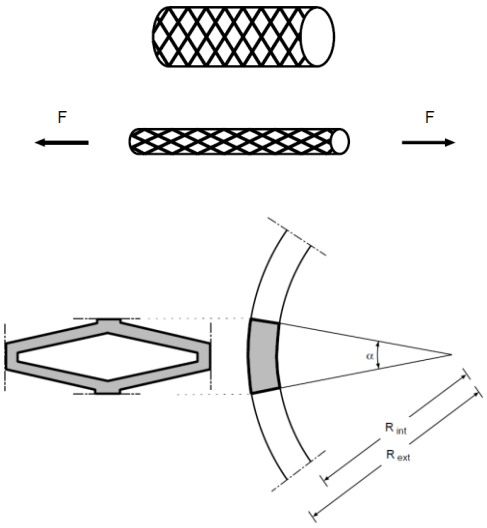

Fig 12: diamond shape stent made of shape memory Nitinol and its side view of cross section

Axi-symmetry is considered and one forth of cross section shown in Figure is enough to be meshed for FE computation.

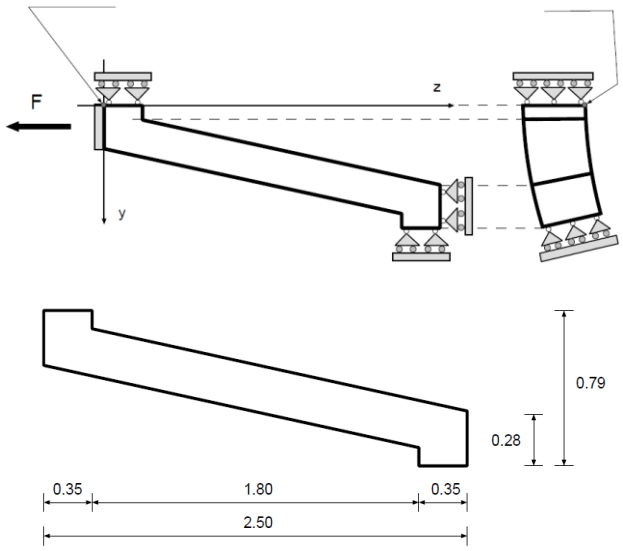

Fig.13: boundary conditions and geometry of section (sizes in millimeter)

$$\alpha = 40^{\circ}, R_{ext} = 2.25\,mm, R_{int} = 2.00\,mm \quad (30)$$

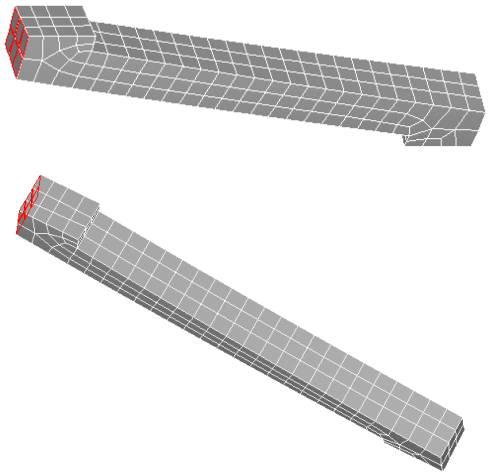

Fig.14: boundary conditions and geometry of section

The initial temperature is $\theta = 22°C$ and kinetic parameters are as follows:

$$P = 2, \dot{\lambda}^{+} = -\dot{\lambda}^{-} = 0.1 \quad (31)$$

The applied force is increased up to 20 N. and then unloading starts. The variation of load versus time and longitudinal and transversal displacements are shown in Figure 15 and 16.

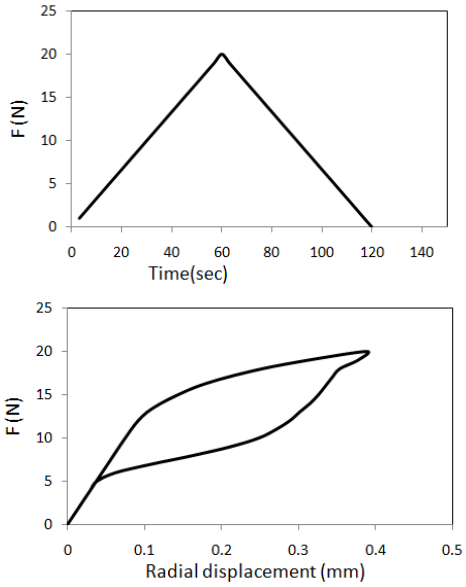

Fig.15: The variation of load/unload versus time and transversal displacement at node A

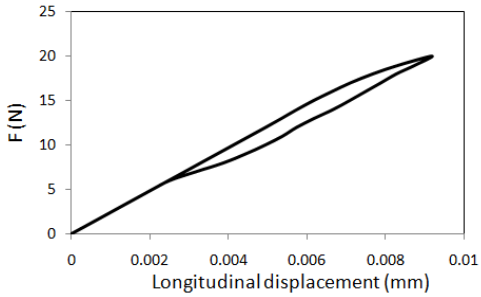

Fig.16: The variation of load versus longitudinal displacement at node A

Figure17 shows the variation of volume fracture factor λ_v contours at different times (24, 30, 36, 42, 48, 54, 60, 92, 102, 108, and 114 seconds, respectively) during loading and unloading.

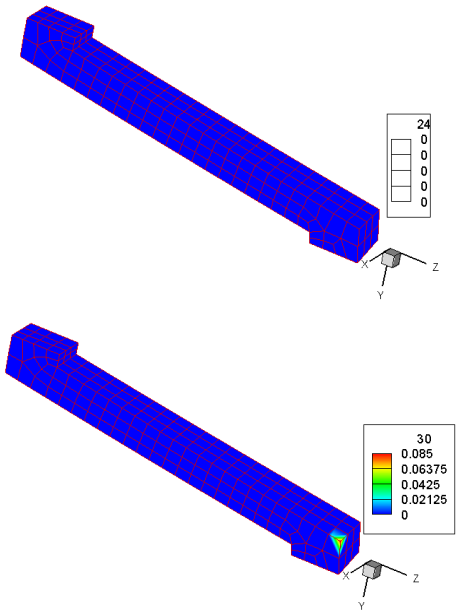

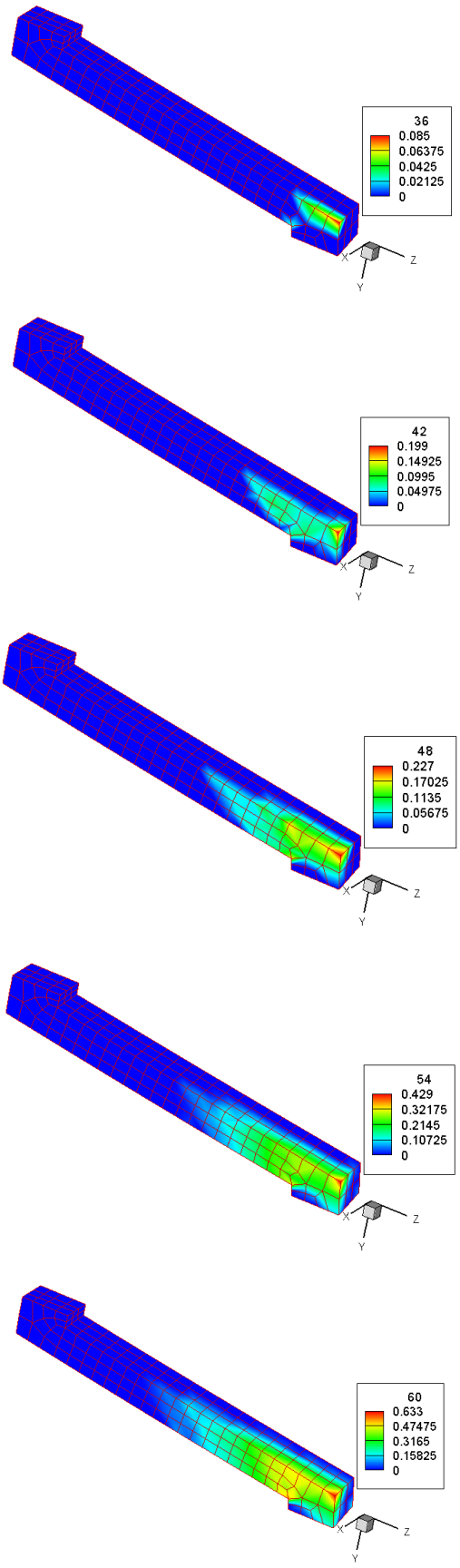

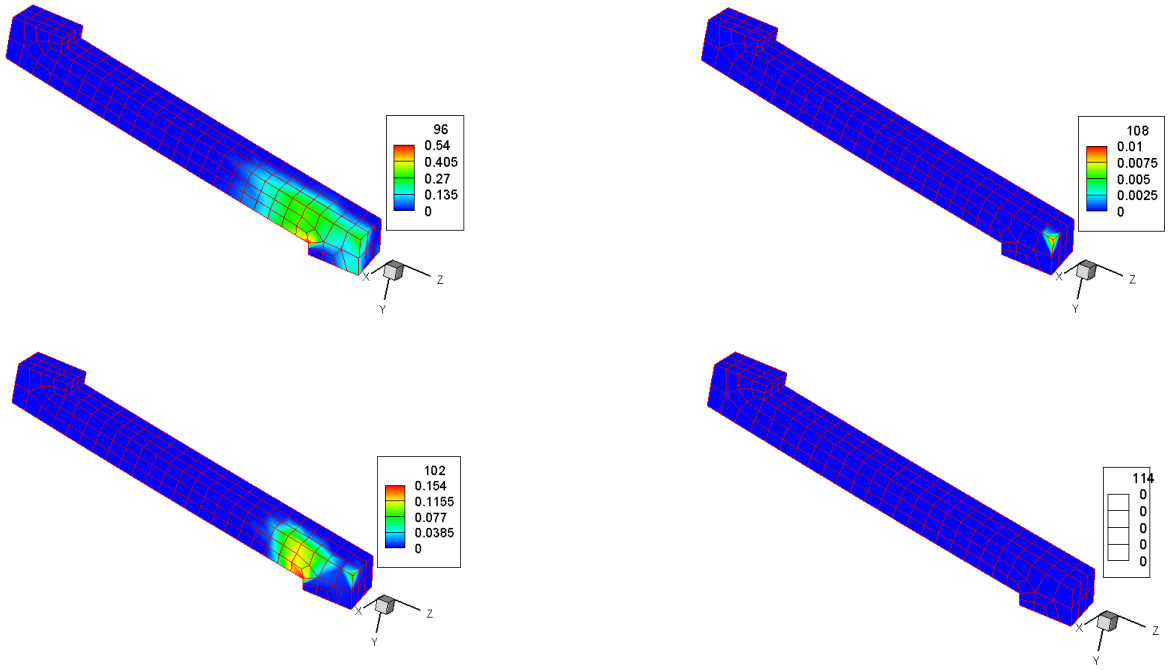

Fig.17: the variation of volume fracture factor λ_v contours at different times during loading and unloading

As it is seen in Figure17, the eccentricity of applied load has created stress concentration at corner due to bending. Therefore, phase change and appearance of martensite strain take place earlier at the shown concentration zones. The start of unloading super elastic behavior causes austenite and leading the elastic and martensite strains to zero. Consequently, stent length returns to initial value. It must be noted that the diamond shape cross section causes a more reduction of diameters due to phase changes.

6. Conclusion

A 3-Dimensional semi-microscopic thermo-mechanical model capable of seeing the effects of the loading rate and predicting phase changes of martensite to austenite and vice versa has been presented for evaluation of stent deformation made of shape memory alloys. The multi-laminate proposed model is also capable of predicting inherent/induced anisotropy effects during the non-linear behavior due to possibility of defining different material parameters for different sampling planes. This model is also able to evaluate the asymmetry in tension and compression and hence, it presents appropriate loops in frequency of loading and unloading. The behavior change due to hydrostatic effect is another feature of this model. Also this model can present deviate from normality in non-proportional biaxial loading case similar to an ideal stentgraft that must be described as being biocompatible, non-carcinogenic, having a stable configuration, flexible, conformable and durable. Regarding the mechanical properties, any ductility and toughness is included in calibration leads to model parameters evaluation. To investigate a stentgraft is compatible with standard angiographic techniques to permit its precise deployment and follow-up within the patient's arteries; it can be numerically modeled to find out weather, it is ideal device, and may also provide information regarding the device's performance to the doctors.

The predicted results of the proposed model along with comparison with the experimental results indicate the power and capability of the proposed model. Therefore, it is can be used to predict the thermo-mechanical behavior of any structure manufactured by shape memory alloys.

References

[1] Johnston, K.W., Robert, B.R., Tilson, M.D., Dhiraj, M.S., Larry, H. and James, C.S. Suggested standards for reporting on arterial aneurysms. Journal of Vascular Surgery, 1991, 13(3), 452-458.

[2] Cao, P., Verzini, F., Rango, P.D., Maritati, G., Pasquale, F.D. and Parlani, G. Different types of thoracic endografts. Journal of Cardiovascular Surgery, 2009, 50(4), 483-492.

[3] Monahan, T.S. and Schneider, D.B. Fenestrated and Branched Stent Grafts for Repair of Complex Aortic Aneurysms. Seminars in Vascular Surgery, 2009, 22(3), 132-139.

[4] Machado, L.G. and Savi, M.A. Medical applications of shape memory alloys. Brazilian Journal of Medical and Biological Research, 2003, 36, 683-691.

[5] Rutherford, R.B. Vascular surgery. (Saunders, 2005). 17 Katzen, B.T. and MacLean, A.A. Complications of endovascular repair of abdominal aortic aneurysms: A review. CardioVascular and Interventional Radiology, 2006, 29(6), 935-946.

[6] Zienkiewicz, O.C., and Pande, G.N., (1977), "Time dependent Multi-laminate Model of Rocks", International Journal of Numerical and Analytical Methods In Geo-mechanics, 1, 219-247.

[7] SADRNEZHAD S.A. & PANDE G.N., A Multilaminate Model For Sand, Proceeding of 3rd International symposium on Numerical Models in Geomechanics, NUMOG-III, 8-11 May 1989, Niagara Falls, CANADA.

[8] Sadrnezhad S.A., (1992), Multilaminate elastoplastic model for granular media, Journal of Engineering, Islamic Republic of Iran, vol.5, Nos.1&2, May, -11.

[9] Sadrnezhad S.A., A Multilaminate Elastic-plastic Model For Liquefaction Of Saturated Sand, Proceeding of the Third International Conference on Seismology and Earthquake Engineering, May 17-19, 1999, I.R.IRAN., p.561-568.

[10] Prat, P. C. and Bazant, Z. P., "Microplane model for triaxial deformation of soils", Journal of Engineering Mechanics-Asce, Vol. 1989, (1989), 139-146.

[11] Bazant, Z. P., Caner, F. C., Carol, I., Adley, M. D. and Akers, S. A., "Microplane model M4 for concrete. I: Formulation with work- conjugate deviatoric stress", Journal of Engineering Mechanics-Asce, Vol. 126, (2000), 944-953.

[12] Sadrnejad, S.A. (1992), 'Induced Anisotropy Prediction Through Plasticity', Proceeding of International Conference on "Engineering Applications of Mechanics", June 9-12, 1992, Teheran-Iran, p.598-605.

[13] Sadrnezhad S.A., (2001), A SEMI-MICRO-MECHANICAL MODEL FOR ANISOTROPY OF SAND, FIRST CONFERENCE ON OPTIMUM USE OF LAND, TEHERAN, IRAN, MARCH 2001, P. 437

[14] Sadrnezhad S.A., (1997), Numerical Identification of Failure Specifications of Soil", 4th International Conference

on Civil Engineering, 4-6 May 1997, Teheran, Iran, p. 100-111.

[15] Sadrnezhad S.A., (1998), Prediction of The Rotation of Principal Stress Axes in Porous Media by Multi-laminate Based Model, Int. Journal of Univ. of Science & Tech. of IRAN, VOL 9, No.1, pp. 15-33.

[16] Rutherford, R.B. Vascular surgery. (Saunders, 2005). 17 Katzen, B.T. and MacLean, A.A. Complications of endovascular repair of abdominal aortic aneurysms: A review. CardioVascular and Interventional Radiology, 2006, 29(6), 935-946.

[17] Puskas, J.E. and Chen, Y. Biomedical application of commercial polymers and novel polyisobutylene-based thermoplastic elastomers for soft tissue replacement. Biomacromolecules, 2004, 5(4), 1141-1154.

[18] A. Roohbakhsh Davaran and S. A. Sadrnejad, (2008), A 3D multi-plane model for shape memory alloys, IJE Trasactions A: Basics Vol.21, No. 1, February 2008.

[19] Amir Sadjadpour and Kaushik Bhattacharya, (2006), A multimechanics inspired constitutive model for shape-memory alloys: The one-dimensional case, Smart. Mat. Struct.accepted for publication, (2006).

[20] Sadjadpour, A. and Bhattacharya, K., (2006), "A micromechanics inspired constitutive model for shape-memory alloys: The one-dimensional case", Smart Mat. Struct., accepted for publication.

[21] Stoeckel, D., Pelton, A. and Duerig, T. Self-expanding nitinol stents: material and design considerations European Radiology, 2004, 14(2), 292-301.

[22] Stoeckel, D. Nitinol medical devices and implants. Minimally Invasive Therapy and Allied Technologies, 2000, 9(2), 81-88.

[23] De la Flor, S., Urbina, C. and Ferrando, F. Effect of mechanical cycling on stabilizing the transformation behaviour of NiTi shape memory alloys. Journal of Alloys and Compounds, 2009, 469(1–2), 343-349.

[24] Medical Device Materials: Proceedings from the Materials & Processes for Medical Devices Conference 2003, 8-10 September 2003, Anaheim, CA, Editor: Shrivastava, S., ASM International, 2003.

[25] Eggeler, G., Hornbogen, E., Yawny, A., Heckmann, A. and Wagner, M. Structural and functional fatigue of NiTi shape memory alloys. Materials Science and Engineering: A, 2004, 378(1–2), 24-33.

[26] Shabalovskaya, S., Anderegg, J. and Van Humbeeck, J. Critical overview of Nitinol surfaces and their modifications for medical applications. Acta Biomaterialia, 2008, 4(3), 447-467.

[27] Lévesque, J., Dubé, D., Fiset, M. and Mantovani, D. Materials and properties for coronary stents. Advanced Materials & Processes, 2004(September), 45-48.

[28] Duerig, T., Pelton, A. and Stöckel, D. An overview of nitinol medical applications. Materials Science and Engineering: A, 1999, 273– 275(0), 149-160.

[29] Kathuria, Y.P. The potential of biocompatible metallic stents and preventing restenosis. Materials Science and Engineering: A, 2006, 417(1– 2), 40-48.

[30] Shih, C.-C., Shih, C.-M., Su, Y.-Y., Su, L.H.J., Chang, M.-S. and Lin, S.-J. Effect of surface oxide properties on corrosion resistance of 316L stainless steel for biomedical applications. Corrosion Science, 2004, 46(2), 427-441.

[31] McNaney, J. M., V. Imbeni, Y. Jung, P. Papadopoulos and R.O. Ritchie, (2003), An experimental study of the superelastic e_ect in a shape-memory Nitinol alloy under biaxial loading, IMech. Mater. 35 969-986.

[32] Hanawa, T. Materials for metallic stents. Journal of Artificial Organs, 2009, 12(2), 73-79.

[33] Niinomi, M. Recent metallic materials for biomedical applications. Metallurgical and Materials Transactions A, 2002, 33(3), 477-486.

[34] Abeyaratne, R., Chu, C., and James, R.D., Kinetics of materials with wiggly energies: theory and application to the evolution of twinning microstructures in a Cu-Al-Ni shape memory alloy. Phil. Mag. A-Physics of Condensed Matter Defects and Mechanical Properties, 73(2): 457-97, 1996.

[35] Patoor E., El Amrani M., Eberhardt A. and Berveiller M., Procs. ESOMAT'94, J. Physique IV, 5, (1995) C2-495-500.

[36] Patoor E., Eberhardt A. and Berveiller M., Arch.Mech. 40 (1988) 775-794.